Adjustable virtual pore-size filter for automated sample preparation using acoustic radiation force

B. Jung, K. Fisher, K. Ness, K. Rose, R. Mariella

May 27, 2008

LAWRENCE
LIVERMORE
NATIONAL
LABORATORY

Disclaimer

This document was prepared as an account of work sponsored by an agency of the United States government. Neither the United States government nor Lawrence Livermore National Security, LLC, nor any of their employees makes any warranty, expressed or implied, or assumes any legal liability or responsibility for the accuracy, completeness, or usefulness of any information, apparatus, product, or process disclosed, or represents that its use would not infringe privately owned rights. Reference herein to any specific commercial product, process, or service by trade name, trademark, manufacturer, or otherwise does not necessarily constitute or imply its endorsement, recommendation, or favoring by the United States government or Lawrence Livermore National Security, LLC. The views and opinions of authors expressed herein do not necessarily state or reflect those of the United States government or Lawrence Livermore National Security, LLC, and shall not be used for advertising or product endorsement purposes.

Adjustable virtual pore-size filter for automated sample preparation using acoustic radiation force

Byoungsok Jung, Karl Fisher, Kevin Ness, Klint A. Rose, and Raymond Mariella Jr.

Lawrence Livermore National Laboratory (LLNL), Livermore, CA 94551, USA

Correspondence
Byoungsok Jung
P.O. Box 808, L-211
Lawrence Livermore National Laboratory (LLNL)
Livermore, CA 94551
USA
Email address: jung7@llnl.gov
Fax: (925) 424-2778

Abstract

We present a rapid and robust size-based separation method for high throughput microfluidic devices using acoustic radiation force. We developed a finite element modeling tool to predict the two-dimensional acoustic radiation force field perpendicular to the flow direction in microfluidic devices. Here we compare the results from this model with experimental parametric studies including variations of the PZT driving frequencies and voltages as well as various particle sizes and compressidensities. These experimental parametric studies also provide insight into the development of an adjustable 'virtual' pore-size filter as well as optimal operating conditions for various microparticle sizes. We demonstrated the separation of *Saccharomyces cerevisiae* and MS2 bacteriophage using acoustic focusing. The acoustic radiation force did not affect the MS2 viruses, and their concentration profile remained unchanged. With optimized design of our microfluidic flow system we were able to achieve yields of > 90% for the MS2 with > 80% of the *S. cerevisiae* being removed in this continuous-flow sample preparation device.

1. Introduction

The development of micro total analysis systems (µTAS) over the last two decades has provided innovative advances in analytical chemistry and biochemistry, clinical diagnostics, and biochemical threats detection [1, 2]. However, handling of "real-world", complex samples (e.g. blood, saliva, nasal washes, sea water, etc.) in labs and clinics often requires slow, manual sample purification and/or preconcentration techniques [3, 4]. Therefore, several approaches for reducing sample preparation to lab-on-a-chip platforms have been investigated including on-chip filtration [5], microdialysis [6], affinity-based extraction [7], immunomagnetic beads [8], and acoustic focusing [9].

Acoustic focusing is particularly effective for manipulating relatively large (> 2 µm) particles suspended in liquid and does not require direct contact with the target particles. Several applications leveraging acoustic radiation forces to manipulating microparticles or biological samples in microfluidic devices have been previously presented. These include acoustic control of particles [10, 11], filtration or trapping of cells [12-14], separation of lipids from blood [15], and continuous separation of mixed microparticles or cells [16, 17].

Acoustic focusing in microfluidic devices is typically realized using a piezoelectric transducer (PZT) to generate acoustic standing waves within the microchannel. These standing waves induce acoustic radiation force fields that direct microparticles towards the nodes (i.e., pressure *minima*) or the anti-nodes (i.e., pressure *maxima*) of the standing waves depending on the relative compressidensity between the particle and the suspending liquid [18]. The compressidensity factor depends on material properties of both

particles and suspending medium, and is given by $A(\rho, \gamma) = \left(\dfrac{5\rho_p - 2\rho_f}{2\rho_p + 2\rho_f} - \dfrac{\rho_f c_f^2}{\rho_p c_p^2} \right)$,

where ρ_p and ρ_f are respectively density of the particle and suspending medium, c_p and c_f are speed of sound in the particle and suspending medium, respectively. For particles larger than 2 µm, the transverse velocities induced in response to these force fields are sufficient to achieve continuous, high throughput separation.

Researchers who attempt viral detection, especially viral discovery, using small samples with potentially low viral titers, generally prefer to avoid the use of physical filters, since there is a significant risk that the virions will adhere to the filter material and, therefore, escape detection by even high-performance assays [19]. Other researchers view this effect as a benefit, for example in the trapping of viruses from drinking water, using electropositive material in the filter [20].

In this work, we develop a microfluidic particle filter that uses acoustic focusing to remove particles above a selected size by adjusting the driving conditions of the transducer. Using the theory described in the following section, we developed a finite element modeling tool to predict the two-dimensional acoustic radiation force field perpendicular to the flow direction in microfluidic devices. We compare results from this model with experimental parametric studies including variations of the PZT driving frequencies and voltages as well as multiple particle sizes and compressidensities. These

experimental parametric studies provide insight into the optimal operating conditions for various microparticle sizes and show the effectiveness of our acoustic device as a filter with an adjustable effective pore size. As a demonstration of this rapid and robust filtering technique, we separated *Saccharomyces cerevisiae* and MS2 bacteriophage with operating conditions optimized via our experimental parametric studies.

2. Theory and Modeling

Typical solutions for the acoustic radiation force in a microfluidic channel are based on one-dimensional approximations for the standing wave field. However, microfluidic channels tend to be on the order of the structural wavelength of the operational frequency and solutions based on these one-dimensional models [21] can have limited accuracy. Modeling approaches that consider two- and three-dimensional operational behavior of the fluid-to-structure interaction of the system are necessary to accurately capture the dynamic behavior of the particles. To predict the motion of particles within the acoustic device, we have applied a method described by Fisher and Miles [18] which combines a finite-difference approximation for the acoustic radiation force with a finite-element model of the pressure field within the fluid. Our 2-D analysis offers an improved method to estimate device performance.

We predict the forces on the particles by first calculating the acoustic pressure field in the fluid generated by the piezoelectric transducer. We use the multi-physics finite element package ATILA (Magsoft, Ballston Spa, NY) to model the two-dimensional fluid, structure and piezoelectric effects in the device. The finite-element solution solves for the pressure field in the fluid and the displacement field in the elastic and piezoelectric structure. To determine the acoustic radiation force in the fluid from the pressure field solution, we use the theoretical acoustic radiation force on a sphere first described by King [22] and extended by Gor'kov [21] and Nyborg [23].

The generalized force field on a small spherical particle ($ka \ll 1$) due to the acoustic standing wave pattern in the fluid is [23]

$$F = \frac{4}{3}\pi a^3 \left\{ B\left(\nabla\langle KE_a \rangle\right) - \left(1 - \gamma\right)\left(\nabla\langle PE_a \rangle\right) \right\}, \qquad (1)$$

where a is the radius of the particle, $k = 2\pi/\lambda_f$ and λ_f is the acoustic wavelength in the fluid. The force, F, is a combination of the gradients of the time-averaged kinetic energy, $\langle KE_a \rangle$, and time-averaged potential energy, $\langle PE_a \rangle$. The contribution of the energies to the overall force is weighted by $B = 3(\rho - \rho_0)/(2\rho + \rho_0)$, a ratio of the fluid density ρ and particle density ρ_0, and $\gamma = \beta/\beta_0$ where β and β_0 are the bulk compressibility of the fluid and particle respectively. The force is proportional to the particle volume, $4/3\pi a^3$. The time-averaged kinetic energy is

$$\langle KE_a \rangle = \lim_{T \to \infty} \frac{1}{T} \int_0^T \frac{\rho}{2} \left\{ \int_{-\infty}^t \frac{1}{\rho} (\nabla p(\tau)) d\tau \right\}^2 dt , \qquad (2)$$

and the time-averaged potential energy is

$$\langle PE_a \rangle = \lim_{T \to \infty} \frac{1}{T} \int_0^T \frac{1}{2\rho c^2} p^2(t) dt . \qquad (3)$$

where T is the time duration (period) of one harmonic wave, and p is the acoustic pressure. The kinetic energy, $\langle KE_a \rangle$ represents the acoustically induced fluid oscillation, time-averaged over one period. The potential energy, $\langle PE_a \rangle$ represents the compression and rarefaction of the fluid, time-averaged over one-period. From the FEM solution for the pressure field, we solve the force field using finite difference approximations for the kinetic and potential energy in terms of the pressure field [18].

3. Experimental Section

Microchip
The microfluidic channels were etched into double-side polished (100) silicon wafers 525 (+/-20) µm thick. The microchannels were patterned using standard photolithography techniques then etched in a DRIE system (ASE® system; Surface Technology Systems, UK) to the appropriate depth (160 to 200 µm). The through-ports were then patterned on the wafer backside and etched through to the front-side channels using DRIE. The borosilicate glass is anodically bonded to the etched silicon to seal the microfluidic channels; designed as an H-filter with two inlets and two outlets. The width and depth of the main separation channel were respectively 500 µm and 200 µm. A PZT (T120-A4E-602; Piezo Systems, Cambridge, MA) is bonded to the backside of silicon layer.

Instrumentation and materials
Our on-chip acoustic filtering system includes acoustics control, fluidics control, and optical detection. The acoustics control consists of a Labview-controlled waveform generator (Model 33220A; Agilent Technologies, Santa Clara, CA), an RF power amplifier (Model 325LA; EIN), and a piezoelectric transducer that is bonded on the backside of the microchip. The fluidics control includes multi-position valves and two-position valves (Valco Instruments, Houston, TX) for automated sequential injection analysis capability, and large volume (1 ml) syringe pumps (Carvo® pump; Tecan, San Jose, CA) for priming and decontamination, and a syringe pump (PHD 2000; Harvard Apparatus, Holliston, MA) for accurate flow controls during acoustic focusing. The detection system consists of an epi-fluorescence microscope (Eclipse 80i; Nikon, Melville, NY) fitted with a wide field-of-view objective (4x or 10x) and a CCD camera (CoolSNAP fx; Photometrics, Tucson, AZ). All modules are controlled by an in-house Labview program.

Red- (emission peak 605 nm) and green (emission peak 515 nm) fluorescent microparticles were purchased from Invitrogen (Carlsbad, CA).

Experimental protocol
Small volume (5-10 µl) of sample is introduced to the inlet of the microchip and injected into the main channel using a syringe pump at a typical flow rate of 20 µl/min. Both inlet channels were filled with samples (i.e., entire channel was uniformly filled with samples) for the characterizations of acoustic focusing performances (Figure 3), and only one inlet channel was filled with samples for the characterizations of separation efficiency (Figures 4, 5). Once a sample plug is introduced and a steady-state flow condition is attained, the PZT is then driven by mono-sinusoidal voltage, $V(2\pi f)$, where the driving frequency, f is first estimated using our simulation and then experimentally determined for an optimal focusing. Fluorescence images were then acquired using a CCD camera. We used an ensemble average of 20 sequential images ($\Delta t = 0.1$ s) to increase signal-to-noise ratio (Figure 1a). All images were normalized using flat- and dark-field images of the microchannel. Fluorescence intensity profile across the microchannel (y-dir) is obtained by averaging the signals along the microchannel direction (x-dir). (Figure 1b)

Figures of merit in acoustic focusing
The efficiency of our acoustic focusing system can be characterized as relative width of focused sample zone compared to the width of microchannel. Figure 1a shows a typical image of focused microbeads (diamter = 2.0 µm) in a 500-µm wide microchannel, where PZT driving frequency and voltage are respectively 1.459 MHz and 6.6 V. Characteristic focused-zone width, W_p is a distance between two y-locations (symmetric on the center of the microchannel) within which the integral of intensity (i.e., concentration) is equal to the half of total intensity value (Figure 1b).

$$\int_{W_p} I_p(y)dy = 0.5 I_{tot} ,$$

where $I_p(y)$ is fluorescence intensity distribution, and I_{tot} is a total intensity value of the sample. Then, a non-dimensional characteristic peak width, δ_1 is given by

$\delta_1 = \dfrac{2W_p}{W_c}$, where W_c is the width of a microchannel. δ_1 is unity for a uniformly

distributed sample (e.g., no acoustic focusing), and is near zero for a tightly focused sample zone for a single-node acoustic focusing, as shown in this paper.

4. Results and Discussion

We simulated the same microchannel geometry and operating conditions for comparison. The surface plot in Figure 2 illustrates the two-dimensional pressure field orthogonal to the flow direction (x-direction) from the simulation. The superimposed vector plot shows the acoustic radiation force in this plane. The dark regions and the light regions respectively represent the nodes and anti-nodes of the acoustic pressure field. The

corresponding force field predicts acoustic focusing at the center of the microchannel, which is confirmed by the experimental results shown in Figure 1a.

We performed experimental parametric studies to optimize our system as well as to validate our modeling. We mainly focused on three key parameters: driving frequency, driving voltage, and particle size. We first examined the efficacy of our system for a broad range of driving frequencies. Figure 3a shows acoustic focusing efficiency $(1-\delta_1)$ as a function of PZT driving frequency. Fluorescence images were detected with a viewing area of 1.0 by 0.5 mm in the object plane at a point 1 mm upstream from the outlet bifurcation. All acoustic focusing reached a steady state within ~20 s after the PZT was activated. The exposure time and frame rate of CCD camera were respectively 10 ms and 10 frames/s. The driving frequency, f, was varied from 1.009 to 1.999 MHz with a 10 kHz discretization. The driving voltage was fixed at 4.76 V. The error bars in this and Figure 4 reflect 90% confidence intervals as determined from thee independent realizations of each condition.

The non-dimensional peak width (δ_1), as described in the previous section, is a figure of merit showing how tightly particles focus around the center line of a microchannel. High acoustic focusing efficiency $(1-\delta_1)$, thereby, represents a tightly focused sample zone. The acoustic focusing efficiency has a maximum value of 0.88 at 1.459 MHz, which was chosen as the optimal operating frequency for this system. The second maximum occurs at 1.409 MHz, but the acoustic focusing efficiency is limited to 0.75. Distinctive focusing of particles $(1-\delta_1 > 0.5)$ was observed only at a frequency range between 1.389 and 1.489 MHz.

Figure 3b shows the effect of driving voltage and particle size on the acoustic focusing efficiency, where we varied the driving voltage from 0 to 9.24 V and selected 5 different sizes of microbeads (0.5, 1.0, 2.0, 3.1, and 5.0 μm in diameter). We fixed the driving frequency at 1.459 MHz and flow rate at 20 μl/min. δ_1 decreased as the driving voltage increased. However, the acoustic focusing does not improve above a certain driving voltage for particles with a diameter 2.0 μm or greater (e.g., δ_1 remains ~ 0.1 above 2.42 V for 5.0 μm particles), and the values of plateau are also different for each diameter of particle (large particles have lower terminal δ_1). We attribute this to the balance between diffusive dispersions and acoustic radiation force.

Experimental results shown in Figure 3b suggest that a size cut-off lies between 1 and 2 μm, where particles do not tightly focus $(\delta_1 < 0.4)$ even for high driving voltages. The optimal driving voltages (i.e., the lowest voltages at which maximum focusing occurs) also varies for different particle sizes, therefore our system provides a robust, tunable size filter. For example, 5.0 μm microparticles can be separated from 2.0 μm microparticles with a driving voltage of 1.93 V. These enable us to use our system as a high throughput, clogless, adjustable 'virtual' pore-size filter.

We then demonstrated the separation of *Saccharomyces cerevisiae* (typical cell size of 4-6 μm depending on the cell growth stage, measured using a Coulter counter) and MS2 bacteriophage (diameter ~30 nm[24]) using acoustic focusing (Figure 4). A mixture of *S.*

cerevisiae and MS2 labeled with Ribogreen was prepared and injected into one inlet of the microchip (i.e., half of the microchannel was filled with the sample). We varied driving voltages from 1.96 to 4.76 V, while fixing the driving frequency at 1.459 MHz and flow rate at 20 μl/min. Signals of (unlabeled) yeast cells and (fluorescent-labeled) MS2 bacteriophages were selectively detected using elastic scattered light microscopy and fluorescence microscopy. Signal intensity profiles were calculated as described in the experimental section, and each of lines represents the average of three realizations. The acoustic radiation force did not affect the MS2 viruses, and their concentration profile remained unchanged. Increased driving voltages enhanced the acoustic focusing of the yeast cells thereby achieving good separation. We are able to achieve yields of > 80% and sample purities of > 90% in this continuous-flow sample preparation device.

We introduce another figure of merit to quantify the efficiency of separation using our acoustic focusing technique. Characteristic focused sample zone width, W_{80} is a distance between two *y*-locations (symmetric on the center of the microchannel, $y = 0$) within which the integral of signal intensity of large particles is 80% of the total intensity of the large particles. The separation efficiency, η_{80} is defined as the percentage of small particles not included in the region of W_{80}, therefore high η_{80} refers to high sample purity (i.e., good separation) of large target particles against small background particles. In Figure 4, the separation of efficiency (η_{80}) is 90% at a driving voltage of 3.86 V.

We also demonstrated the separation of mixtures of microparticles with various sizes using acoustic focusing. Figure 5 shows separation efficiency (η_{80}) of various mixtures of microparticles and a mixture of yeast and MS2 depending on the driving voltage. Six sets of mixture were chosen (5 μm and 20 nm, 5 μm and 0.5 μm, 5 μm and 2.0 μm, 3.1 μm and 20 nm, 3.1 μm and 0.5 μm, and 3.1 μm and 2.0 μm), and small- and large microbeads were respectively red- (emission peak 580 nm) and green (emission peak 515 nm) fluorescent particles. Driving voltages were varied from 1.02 to 3.83 V, and driving frequency was fixed at 1.459 MHz.

For the first three sets of mixtures (black circle: 5 μm and 20 nm, gray square: 5 μm and 0.5 μm, and white triangle: 5 μm and 2.0 μm), the size difference between target (i.e., large particles, focusing needed) particles and smaller background particles are relatively big, and show good separation (> 80% removal of small particles) at 2.89 V. The mixture of 3.1 μm and 20 nm (gray circle), and the mixture of 3.1 μm and 0.5 μm (white square) also show moderate separation (~70% removal of small particles) at 3.83 V. However, separation efficiency of a mixture with the smallest size difference (black triangle: 3.1 μm and 2.0 μm) is limited to 51% at 2.89 V, and does not improve with higher acoustic focusing power.

5. Summary

Acoustic focusing provides rapid and robust manipulation of suspended particles and can be easily integrated with other μTAS functionalities. The 2D numerical simulation using

FEM yields first order estimate of operation conditions for a PZT and predicts the location of focused particles in the microchannel.

We performed an experimental parametric study focused on the variation of particle size, driving voltage, and driving frequency. Consistent with the simulation, we found that the polystyrene microparticles and yeast cells focus at the nodes of acoustic standing waves located at the center of the microchannel. We also found that particles larger than 2 μm in diameter effectively focused. Therefore, our device provides a clogless filter for large particles (e.g., cells, debris) from complex biological samples. The focusing efficiency of particles depends on the driving voltage as well as particle size. These results give insight into adjustable 'virtual' pore-size filter (i.e., no physical filter in the microchannel), where the virtual pore-size can be easily varied by adjusting the driving voltage of PZT.

Separation of yeast cells from MS2 viruses was demonstrated with maximum recovery of 90% for the MS2 with 80% removal of *S. cerevisiae*. We also analyzed the separation of mixtures of microparticles by adjusting the driving voltage, and the results show good separation of cell-sized particles (3-5 μm) against virus-like (40 nm) and bacteria-like (0.5 μm) particles. Future work will include the development and validation of more comprehensive models for the acoustic focusing and further applications of our acoustic focusing protocol to 'real' biological samples.

Figure 1. A representative acoustic focusing of microparticles (diameter of 2.0 µm). (a) Fluorescence images of focused microparticles. The driving frequency and voltage were 1.459 MHz and 6.60 V, respectively. The microparticles tightly focus (full width half maximum (FWHM) ~30 µm) less than 30 s after the initiation of the acoustic field. Flow rate was 20 µl/min, and a 4x objective (N.A. = 0.1) was used. (b) Intensity profile across the microchannel (*y*-direction) obtained by averaging intensity along *x*-direction (1 mm long).

(a)

(b)
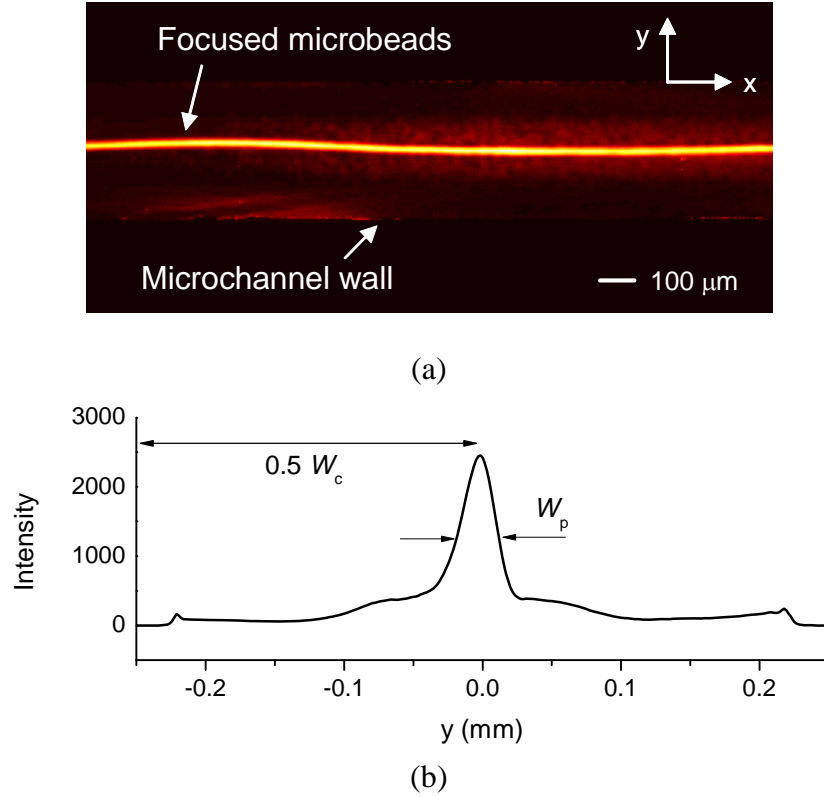
Figure 2. Two-dimensional numerical estimate of the acoustic pressure field and the acoustic radiation force field shown for a cross section of the microchannel. The dark regions and the light regions represent nodes (low acoustic pressure) and anti-nodes (high acoustic pressure) in the acoustic pressure field, respectively. The driving frequency was set to 1.4809 MHz. The acoustic radiation force field (vector plot) predicts a strong acoustic focusing at the nodes (the center of the microchannel).
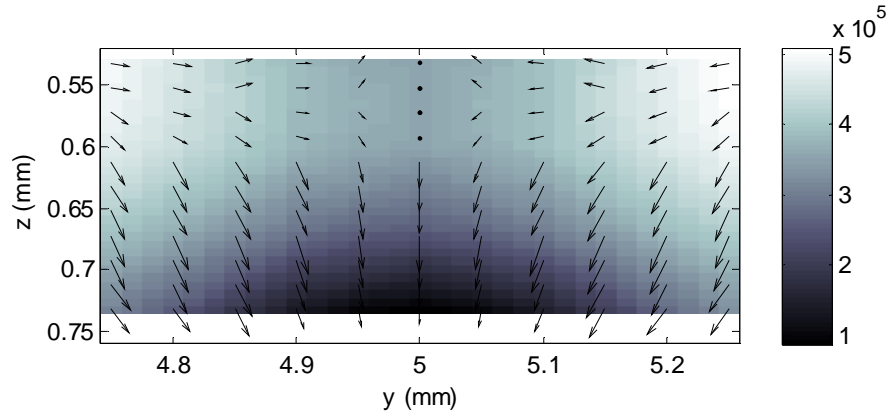
Figure 3. (a) Acoustic focusing efficiency as a function of driving frequency. Microparticles with a diameter of 3.1 μm were used. The driving voltage applied to a PZT was 4.76 V, and flow rate was fixed at 20 μl/min. (b) Acoustic focusing efficiency as a function of driving voltage. Root-mean-square voltage applied to a PZT (V_{rms}) was varied from 0 to 9.25 V. Microbeads with a diameter of 0.5 μm (white circle), 1.0 μm (gray triangle), 2.0 μm (white square), 3.1 μm (gray circle), and 5.0 μm (white triangle) were used. Baclight-labeled yeast (black diamond) was also tested. The driving frequency was 1.459 MHz, and flow rate was 20 μl/min.
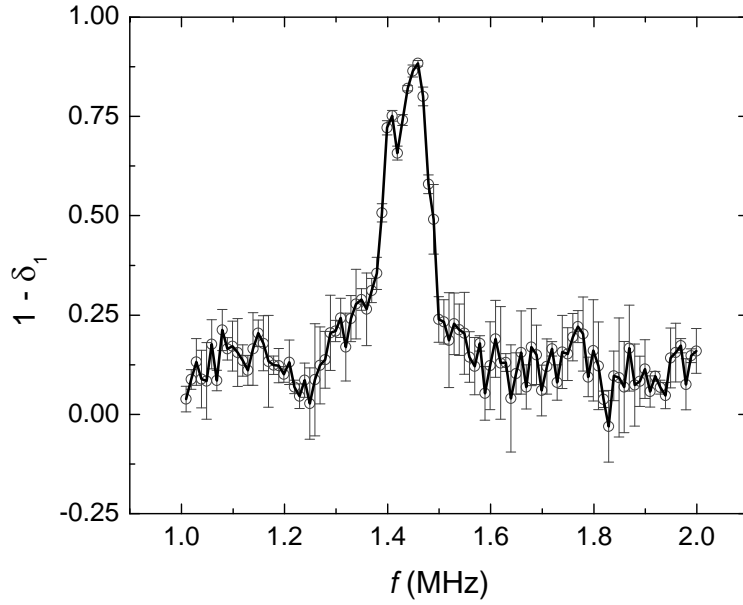
(a)
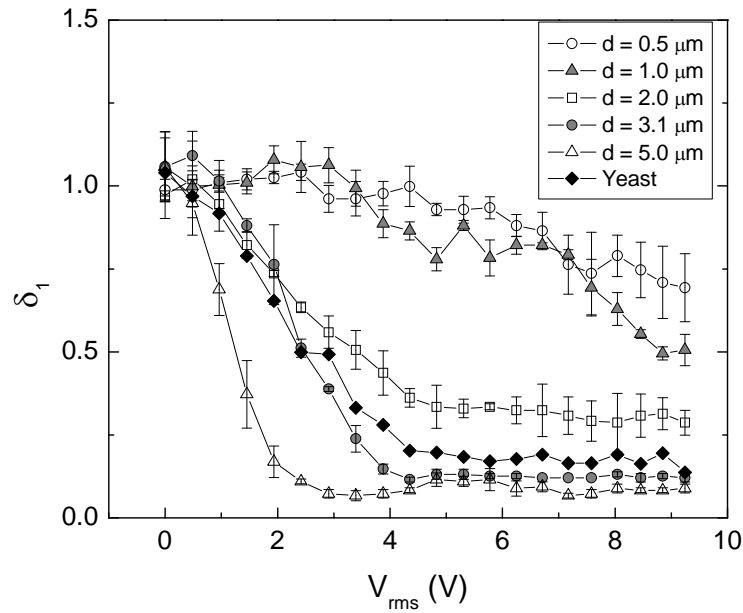
(b)

Figure 4. Separations of a mixture of yeast cells and MS2 viruses. Concentration profiles (normalized intensity) across the microchannel width direction (*y*) are shown for the driving voltages from 1.96 to 4.76 volts. The driving frequency and flow rate was 1.459 MHz and 20 μl/min, respectively. Samples were initially introduced only at the right half of the microchannel.
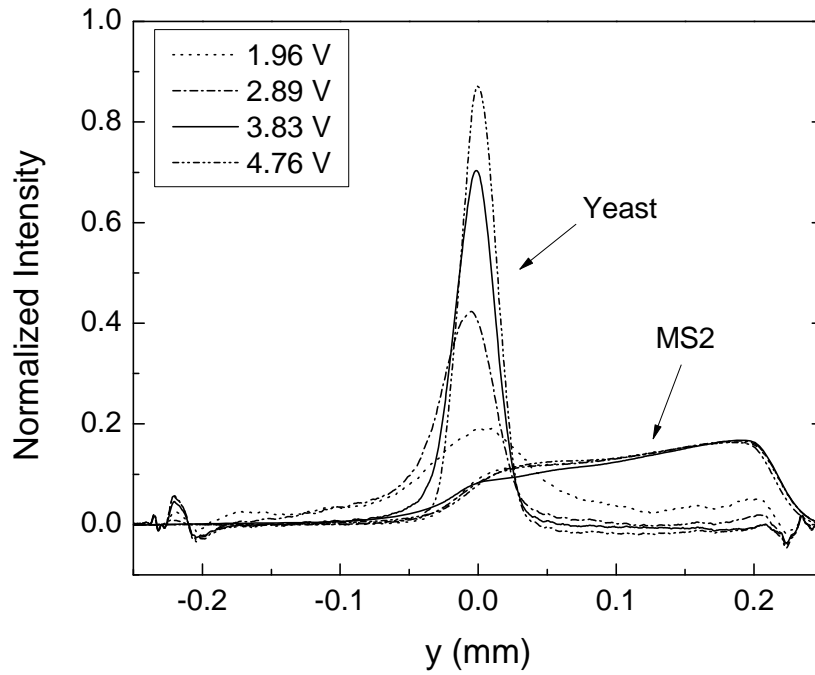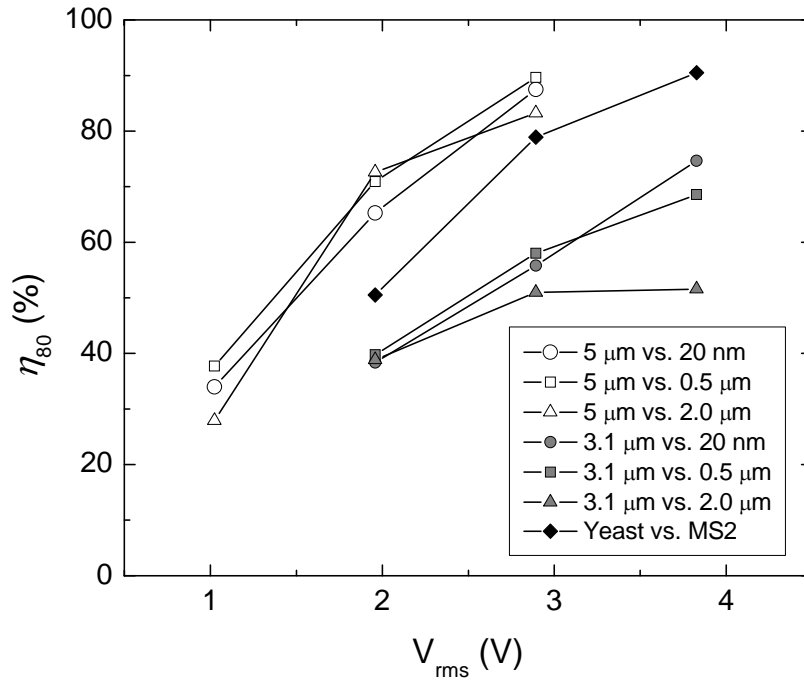
Figure 5. Sample separation efficiency for various mixtures of microbeads and a mixture of yeast and MS2. Separation efficiency (η_{80}) represents the percentage of background (smaller) particles outside of focused zone of target (larger) particles. Driving voltages applied to a PZT were varied from 1.02 to 3.83 volts, and driving frequency was fixed at 1.459 MHz.

References

(1)   Auroux, P. A.; Iossifidis, D.; Reyes, D. R.; Manz, A. *Analytical Chemistry* **2002**, *74*, 2637-2652.

(2)   Reyes, D. R.; Iossifidis, D.; Auroux, P. A.; Manz, A. *Analytical Chemistry* **2002**, *74*, 2623-2636.

(3)   Ramsey, J. M. *Nature Biotechnology* **1999**, *17*, 1061-1062.

(4)   Crevillen, A. G.; Hervas, M.; Lopez, M. A.; Gonzalez, M. C.; Escarpa, A. *Talanta* **2007**, *74*, 342-357.

(5)   Yuen, P. K.; Kricka, L. J.; Fortina, P.; Panaro, N. J.; Sakazume, T.; Wilding, P. *Genome Research* **2001**, *11*, 405-412.

(6)   Xu, N. X.; Lin, Y. H.; Hofstadler, S. A.; Matson, D.; Call, C. J.; Smith, R. D. *Analytical Chemistry* **1998**, *70*, 3553-3556.

(7)   Yu, C.; Davey, M. H.; Svec, F.; Frechet, J. M. J. *Analytical Chemistry* **2001**, *73*, 5088-5096.

(8)   Liu, R. H.; Yang, J. N.; Lenigk, R.; Bonanno, J.; Grodzinski, P. *Analytical Chemistry* **2004**, *76*, 1824-1831.

(9)   Hawkes, J. J.; Limaye, M. S.; Coakley, W. T. *Journal of Applied Microbiology* **1997**, *82*, 39-47.

(10)   Nilsson, A.; Petersson, F.; Jonsson, H.; Laurell, T. *Lab on a Chip* **2004**, *4*, 131-135.

(11)   Oberti, S.; Neild, A.; Dual, J. *Journal of the Acoustical Society of America* **2007**, *121*, 778-785.

(12)   Evander, M.; Johansson, L.; Lilliehorn, T.; Piskur, J.; Lindvall, M.; Johansson, S.; Almqvist, M.; Laurell, T.; Nilsson, J. *Analytical Chemistry* **2007**, *79*, 2984-2991.

(13)   Hawkes, J. J.; Coakley, W. T. *Sensors and Actuators B-Chemical* **2001**, *75*, 213-222.

(14)   Yasuda, K.; Haupt, S. S.; Umemura, S.; Yagi, T.; Nishida, M.; Shibata, Y. *Journal of the Acoustical Society of America* **1997**, *102*, 642-645.

(15)   Petersson, F.; Nilsson, A.; Holm, C.; Jonsson, H.; Laurell, T. *Analyst* **2004**, *129*, 938-943.

(16)   Kapishnikov, S.; Kantsler, V.; Steinberg, V. *Journal of Statistical Mechanics-Theory and Experiment* **2006**, -.

(17)   Petersson, F.; Aberg, L.; Sward-Nilsson, A. M.; Laurell, T. *Analytical Chemistry* **2007**, *79*, 5117-5123.

(18)   Fisher, K.; Miles, R. *Journal of the Acoustical Society of America* **2008**, *123*, 1100-1104.

(19)   DeRisi, J.; Private Communication, 2008.

(20)   Lambertini, E.; Spencer, S. K.; Bertz, P. D.; Loge, F. J.; Kieke, B. A.; Borchardt, M. A. *Applied and Environmental Microbiology* **2008**, *74*, 2990-2996.

(21)   Gor'kov, L. P. *Soviet Physics Doklady* **1962**, *6*, 773-775.

(22)   King, L. V. *Proceedings of the Royal Society of London. Series A, Mathematical and Physical Sciences* **1934**, *147*, 212-240.

(23)   Nyborg, W. L. *Journal of the Acoustical Society of America* **1967**, *42*, 947-952.

(24)   Anobom, C. D.; Albuquerque, S. C.; Albernaz, F. P.; Oliveira, A. C.; Silva, J. L.; Peabody, D. S.; Valente, A. P.; Almeida, F. C. L. *Biophysical Journal* **2003**, *84*, 3894-3903.